PHYSICAL REVIEW B **102**, 085415 (2020)

Design and analysis of nanopatterned graphene-based structures for trapping applications

Achiles F. da Mota,[1] Augusto Martins,[2] John Weiner,[3] Philippe Courteille,[3] Emiliano R. Martins,[2] and Ben-Hur V. Borges[2]
[1] *Department of Electrical Engineering, University of Brasília (UnB), Brasilia 70910-900, Brazil*
[2] *Department of Electrical and Computer Engineering, University of São Paulo, CEP 13566-590, São Carlos, SP, Brazil*
[3] *Physics Institute of São Carlos, University of São Paulo, CEP 13566-590, São Carlos, SP, Brazil*

(Received 28 April 2020; accepted 24 July 2020; published 12 August 2020)

Trapping, levitating, and manipulating nanoscale objects with light forces shaped by patterned metamaterials continues to hold great interest for optical and condensed matter physics and engineering. Successful developments to date have concentrated on constraining movement only in one dimension, along the vertical axis to a material plane. Here we propose a realistic structure, consisting of alternating layers of graphene and dielectric, and periodically nanopatterned on the surface, that is capable of levitating and trapping nanoscale particles in two dimensions: one perpendicular and one parallel to the material plane. Repulsive forces arising from high- k modes of the metamaterial provide particle levitation along the vertical axis. At the point where this repulsive force balances the downward gravitational force, the particle is trapped at stable equilibrium. Periodic nanopatterning in the metamaterial surface furnishes the second, horizontal axis constraining particle motion. We show that the equilibrium position above the surface can be controlled by adjusting both the Fermi level and the number of graphene layers. Furthermore, to explicate the role of the high-k modes in generating the repulsive forces, we also propose a semianalytical method to calculate both the potential well and the forces generated by dipole radiation above the nanopatterned surface.

DOI: 10.1103/PhysRevB.102.085415

I. INTRODUCTION

The use of optical forces produced by electromagnetic radiation has been extensively explored by the scientific community over the past decades to control the position of small particles, such as cells, viruses, molecules, or atoms [1–14]. The precise control of the particle position allows trapping in specific locations, as is desirable for optical cooling [1], optical trapping [2], quantum computing [7], lab-on-a-chip [8], and electromagnetic levitation [9–13], among other applications [14]. Particle optical trapping is achieved usually with a potential minimum generated by optical forces exerted by an external light source [5,6,15–23]. The field distribution required to create a stable potential well can be produced, for instance, by Gaussian beams [16,17,22], waveguides [19,20], and plasmonic structures [23]. Nonetheless, all these approaches need complex optical setups [16–23] with limited control of the particle position [24].

Fortunately, the optical setups can be greatly simplified if the force gradients are produced by the radiation scattered by the particle itself [6–9,19–25]. A promising way of shaping the potential gradients consists in letting the radiation scattered by the particle interact with nearby structures or interfaces [10,26]. When the structure is composed of conventional materials, such as metals and dielectrics, the resulting force is attractive; i.e., it acts to pull the particles toward the surface [13,24,27]. In contrast, artificial materials (or metamaterials) can successfully produce repulsive forces strong enough to prevent the particle from touching the surface [6–9,19–25,28,29]. Producing repulsive forces with particle self-radiation, as opposed to conventional approaches, allows particle levitation and trapping with a plane wave pumping the emitters.

According to [13], in the quasistatic regime ($k_x \gg k_0$, where $k_0 = 2\pi/\lambda$, λ is the wavelength, and k_x is the parallel component of the wave vector $\mathbf{k}$), repulsive forces are obtained when the particle is at close distance from a structure ($<\lambda/20$) whose s- and p-polarization[1] reflection coefficients have negative real parts ($Re\{R_{s,} R_p\} < 0$). Assuming a particle in free space above a homogeneous biaxial structure with permittivity and permeability tensors defined as $\bar{\boldsymbol{\varepsilon}} = \mathrm{diag}[\varepsilon_\parallel \quad \varepsilon_\parallel \quad \varepsilon_\perp]$ and $\bar{\boldsymbol{\mu}} = \mathrm{diag}[\mu_\parallel \quad \mu_\parallel \quad \mu_\perp]$, the s- and p-polarized waves' contributions to the force become repulsive when $|\sqrt{\mu_\perp \mu_\parallel}| < 1$ and $|\sqrt{\varepsilon_\perp \varepsilon_\parallel}| < 1$. In this scenario, the authors of [13] have considered subwavelength particles that behave essentially as electric dipoles. Since p waves dominate the radiation of electric dipoles [30,31] the condition $|\sqrt{\varepsilon_\perp \varepsilon_\parallel}| < 1$ is usually sufficient to guarantee repulsive forces (see Appendix A for details).

There are several design approaches to metamaterials with $\varepsilon_\perp$ and $\varepsilon_\parallel$ close to zero [32–34], but the simplest uses a planar stack of alternating metal/dielectric layers [35–39]. By fine-tuning the material layers and thicknesses, it is possible to control both $\varepsilon_\perp$ and $\varepsilon_\parallel$ [35–39]. Although metamaterials with $|\sqrt{\varepsilon_\perp \varepsilon_\parallel}| < 1$ are not difficult to design, these media present strong spatial dispersion for evanescent waves ($|k_x| \gg k_0$), that gives rise to a spatial frequency cutoff k_c,

---

[1] s- and p-polarized waves have the electric field perpendicular and parallel, respectively, to the optical axis.

2469-9950/2020/102(8)/085415(13)

where $|\sqrt{\varepsilon_{\perp}(k_x)\varepsilon_{\parallel}(k_x)}| > 1$ for $|k_x| > k_c$ [40–44]. This feature becomes a critical issue if the particle is close to the surface, where the evanescent wave coupling is strong. In this condition, the repulsive force from waves below cutoff ($|k_x| < k_c$) is overcome by the attractive forces from waves above cutoff ($|k_x| > k_c$) that pull the particle down toward the surface.

One approach to increase k_c is to reduce the layer thickness [41]. Thus, some authors have proposed replacing the metal layers by two-dimensional (2D) materials, such as graphene or boron nitrite, because the layers of these materials are atomically thin [45]. Particularly for graphene, the spatial dispersion becomes negligible if λ is much longer than the Fermi wavelength ($\lambda_F = 2\pi/k_f = \sim$4–10 nm, where k_f is the Fermi wave vector) [46]. Moreover, graphene offers the opportunity of controlling the repulsive force magnitude and equilibrium distance (through levitation, where attractive, repulsive and gravitational forces balance) by tuning the Fermi level (E_F) [46–48].

In this context, we propose here a graphene-based structure capable of trapping small particles above the surface and demonstrate how to control the particle-surface distance by manipulating the graphene conductivity. In addition to trapping the particle along the structure normal axis (particle levitation), we also utilize nanopatterns to lock them along one of the in-plane axes. The nanopatterns allow the particle to be confined in small regions, resulting in enhanced position control. Moreover, we calculate the force spatial-frequency spectrum to demonstrate both the influence of high-k modes and how the patterns unbalance the force to create lateral forces that trap the particle along the x axis. This paper reports a practical structure capable of using the particle scattered radiation to create a two-dimensional (2D) potential well. We also propose a semianalytical procedure to calculate the optical forces of a dipole above a nanopatterned structure (along one or two axes). Despite previous analytical techniques proposed to calculate the recoil forces in several scenarios [6–9,19–25], our semianalytical procedure is tailored for detailed and accurate calculation of the optical forces and electric potential of a point dipole above nanopatterned structures.

This paper is organized as follows. Section II presents the mathematical formalism describing the potential (U) and the force (**F**) acting on a particle above a general nanopatterned structure. In Sec. III, we describe the optimization of both the Fermi potential and the number of graphene layers to obtain the potential energy profile required for trapping particles. We also discuss the influence of the high-k modes on the depth of the potential well. In Sec. IV, we investigate the influence of nanopatterns on the potential as well as the role played by the grooves on the lateral force responsible for confining the particle along the x axis. Finally, we make some concluding remarks in Sec. V.

II. MATHEMATICAL MODEL

There is consensus in the literature, and also assumed here, that small particles behave as electric point dipoles governed by Maxwell's equations when they are far from any resonance [6–9,19–25]. The time-averaged optical force (**F**) due to an electric field $\mathbf{E_t} = E_x\mathbf{x} + E_y\mathbf{y} + E_z\mathbf{z}$ acting on a dipole located at position $\mathbf{r_d}$ is given by [47]

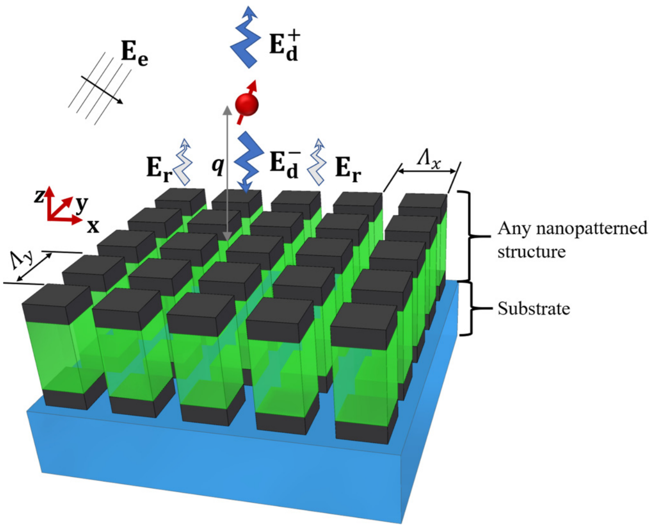

FIG. 1. Nanopatterned structure with periods Λ_x and Λ_y along the x and y directions, respectively, used here as a model for calculating the electric POTENTIAL. The dipole is excited by an external plane wave and scatters light toward the $+z$ ($\mathbf{E_d^+}$) and $-z$ ($\mathbf{E_d^-}$) directions. $\mathbf{E_d^-}$ is reflected by the patterned structure creating a potential well.

$$\langle \mathbf{F}(\mathbf{r_d})\rangle = \frac{1}{2}\mathrm{Re}\left\{\sum_{b=x,y,z} p_b^{*}\nabla E_b(\mathbf{r_d})\right\} - \mathbf{F_g}, \tag{1}$$

where p_b is the b component of the dipole momentum **p** ($b = x,\ y,$ or z) and $\mathbf{F_g}$ is the gravity force ($|\mathbf{F_g}| = mg$, where m is the particle mass and g the gravity acceleration constant, $g \cong 9.8\ \mathrm{m/s^2}$). In Eq. (1), **p** is the sum of the dipole moment generated by means of an external light source and the dipole fluctuations due to the temperature [49–51]. Nonetheless, these fluctuations that give rise to the Casimir-Polder interactions are small compared to the external light dipole excitation. Thus, the fluctuation contributions to **p** will be neglected henceforth. In the quasistatic approximation, the dipolar force is also defined as the negative gradient of the potential energy U, or $\mathbf{F} = -\nabla U$ [52]; thus,

$$U(\mathbf{r_d}) = -\frac{1}{2}\mathrm{Re}\left\{\sum_{b=x,y,z} p_b^{*}E_b(\mathbf{r_d})\right\} + U_g(q) + cte, \tag{2}$$

where $U_g = mgq$ is the gravitational potential energy and q is the distance of the dipole from the surface. According to (1) and (2), to calculate **F** and U it is necessary first to calculate the total electric field at the dipole position. Thus, consider a dipole embedded in medium 1 (with permittivity ε_1) above a nanopatterned structure with periods Λ_x and Λ_y along the x and y directions, respectively, as depicted in Fig. 1. The total electric field acting on the particle is

$$\mathbf{E_t}(\mathbf{r_d}) = \mathbf{E_d}(\mathbf{r_d}) + \mathbf{E_r}(\mathbf{r_d}) + \mathbf{E_e}(\mathbf{r_d}), \tag{3}$$

where $\mathbf{E_e}$ is the electric field that excites the dipole, $\mathbf{E_d}$ is the electric field scattered by the dipole, $\mathbf{E_r}$ is the electric field reflected by the nanopatterned structure, and $\mathbf{r_d} = q\mathbf{z}$ is the dipole position. In addition, there is also the electric field at the particle position induced by current fluctuations at the structure surface [49–51]. Nonetheless, these fluctuations that also give rise to the Casimir-Polder interactions are negligible compared to the external light electric field at the distances pertinent to this study. Therefore, they are not taken further into consideration. Based on (3), the potential can be decomposed as

$$U(\mathbf{r_d}) = U_d + U_e + U_r + U_g(q) + cte, \tag{4}$$

where U_d, U_e, and U_r are the potentials generated by $\mathbf{E_d}$, $\mathbf{E_e}$, and $\mathbf{E_r}$, respectively. The 2D Fourier transform (FT) of the electric field radiated by the dipole toward the $+\mathbf{z}$ ($\mathbf{E_d^{FT,+}}$) and $-\mathbf{z}$ ($\mathbf{E_d^{FT,-}}$) directions is written as [31,53]

$$\begin{aligned}\mathbf{E_d^{FT,\xi}}(\mathbf{k}_{||}, z) = i\frac{\omega\mu_1}{4\pi}e^{i\xi k_z(z-q)}[\mathbf{P_s}(\mathbf{k}_{||}) \otimes \mathbf{L_s}(\mathbf{k}_{||}, z-q)\\ + \mathbf{P_p}(\mathbf{k}_{||}) \otimes \mathbf{L_p}(\mathbf{k}_{||}, z-q)]\mathbf{p},\end{aligned} \tag{5}$$

where ω is the angular frequency, μ_1 is the permeability of medium 1, $k_1 = |\mathbf{k_1}| = |k_x\mathbf{x} + k_y\mathbf{y} + \xi k_z\mathbf{z}|$ is the magnitude of the wave number in medium 1, $\mathbf{k}_\parallel = k_x\mathbf{x} + k_y\mathbf{y}$ is the parallel component of $\mathbf{k_1}$, $\otimes$ is the outer product symbol, and $\xi = 1$ or -1 for waves propagating along the $+z$ or $-z$ direction, respectively. Vectors $\mathbf{L}_\chi$ and $\mathbf{P}_\chi$ in (4), with χ denoting wave polarization ($\chi = s$ or p), are as follows,

$$\mathbf{L_s}(\mathbf{k}_{||}, z-h) = \frac{e^{\xi i k_z(z-q)}}{k_z|\mathbf{k}_{||}|}[k_y \quad -k_x \quad 0]^{\mathrm{T}}, \tag{6}$$

$$\mathbf{L_p}(\mathbf{k}_{||}, z-h) = \frac{e^{\xi i k_z(z-q)}}{k_1|\mathbf{k}_{||}|}\left[k_x \quad k_y \quad -\xi\frac{|\mathbf{k}_{||}|^2}{k_z}\right]^{\mathrm{T}}, \tag{7}$$

$$\mathbf{P_s}(\mathbf{k}_{||}) = \frac{1}{|\mathbf{k}_{||}|}[k_y \quad -k_x \quad 0]^T, \tag{8}$$

$$\mathbf{P_p}(\mathbf{k}_{||}) = \frac{1}{k_1|\mathbf{k}_{||}|}[k_xk_z \quad k_yk_z \quad -\xi|\mathbf{k}_{||}|^2]^T, \tag{9}$$

where the superscript T denotes transposed matrix. The vectors $\mathbf{L}_\chi$ are related to the amplitude of $\mathbf{E_d^{FT,\xi}}$ while the vectors $\mathbf{P}_\chi$ affect the decomposition of the electric field into its x, y, and z components [31]. As shown in Fig. 1, $\mathbf{E_d^-}$ is reflected at the surface of the nanopatterned structure therefore generating $\mathbf{E_r}$, which in turn is calculated via the Fourier transform of $\mathbf{E_r^{FT}}$ as follows [31],

$$\begin{aligned}&\mathbf{E_r^{FT}}(\mathbf{k}_{||}, z)\\ &= i\frac{\omega^2\mu_1}{4\pi}\left(\left\{\sum_{b=x,y,z} p_b\big[R^b_{s,s}(\mathbf{k}_\parallel) + R^b_{p,s}(\mathbf{k}_\parallel)\big]\right\}\mathbf{P_s}\big(\mathbf{k}_\parallel\big)\right.\\ &\quad\left. + \left\{\sum_{b=x,y,z} p_b\big[R^b_{s,p}(\mathbf{k}_\parallel) + R^b_{p,p}(\mathbf{k}_\parallel)\big]\right\}\mathbf{P_p}(\mathbf{k}_\parallel)\right)e^{ik_zz},\end{aligned} \tag{10}$$

$$R^z_{p,\sigma}(\mathbf{k}_{||}) = -\sum_{j,m=-\infty}^{\infty}\frac{|\mathbf{k}_\parallel^{\mathbf{j,m}}|}{k_z^{j,m}k_1}e^{ik_z^{j,m}q}r^{j,m}_{p,\sigma}(\mathbf{k}_\parallel^{\mathbf{j,m}}), \tag{11}$$

$$R^z_{s,\sigma}(\mathbf{k}_{||}) = 0, \tag{12}$$

$$R^{x(y)}_{s,\sigma}(\mathbf{k}_{||}) = \sum_{j,m=-\infty}^{\infty}\frac{k^{m(j)}_{y(x)}}{k_z^{j,m}|\mathbf{k}_\parallel^{\mathbf{j,m}}|}e^{ik_z^{j,m}q}r^{j,m}_{s,\sigma}(\mathbf{k}_\parallel^{\mathbf{j,m}}), \tag{13}$$

$$R^{x(y)}_{p,\sigma}(\mathbf{k}_{||}) = \sum_{i,m=-\infty}^{\infty}\frac{k^{j(m)}_{x(y)}}{k_1|\mathbf{k}_\parallel^{\mathbf{j,m}}|}e^{ik_z^{j,m}q}r^{j,m}_{p,\sigma}(\mathbf{k}_\parallel^{\mathbf{j,m}}), \tag{14}$$

$$\begin{aligned}k_x^i &= k_x - jK_x\\ k_y^m &= k_y - mK_y\\ \mathbf{k}_\parallel^{\mathbf{j,m}} &= k_x^j\mathbf{x} + k_y^m\mathbf{y}\\ k_z^{j,m} &= \sqrt{k_1^2 - |\mathbf{k}_\parallel^{\mathbf{j,m}}|^2},\end{aligned} \tag{15}$$

where $r^{j,m}_{\chi,\sigma}$ is the reflection coefficient of the (j,m) diffraction order along the (x, y) axis for a χ-polarized incident wave with vector $\mathbf{k}_\parallel^{\mathbf{j,m}}$ reflected with σ polarization ($\chi, \sigma = s$ or p), K_x and K_y are the nanopatterned reciprocal lattice vector amplitudes in the x and y directions, respectively [$K_{x(y)} = 2\pi/\Lambda_{x(y)}$, where $\Lambda_{x(y)}$ is the structure periodicity along the x (y) axis]. We use the semianalytical rigorous coupled wave analysis (RCWA) method to calculate the reflection coefficients [54–57]. After calculating $\mathbf{E_d^{FT,\xi}}$ and $\mathbf{E_r^{FT}}$, the spatial distribution of $\mathbf{E_d}$ and $\mathbf{E_r}$, required to calculate U in (2) and (4), can be found using the 2D inverse FT as follows:

$$\begin{aligned}&\mathbf{E}_\alpha(\mathbf{r}) = \frac{1}{2\pi}\int_{-\infty}^{\infty}\int_{-\infty}^{\infty}\mathbf{E}_\alpha^{\mathbf{FT}}(\mathbf{k}_{||}, z)e^{i(k_xx+k_yy)}dk_xdk_y,\\ &\alpha = \mathbf{r} \;\text{ or }\; \mathbf{d}.\end{aligned} \tag{16}$$

In short, the first step to obtain the total force acting on a particle above a nanopatterned structure is to calculate the dipole emitted ($\mathbf{E_d}$) and reflected ($\mathbf{E_r}$) fields, followed by substitution into (3) and (2), and finally (1). Notice that the spatial distribution of the excitation field ($\mathbf{E_e}$), required in (3), is already known.

Another important parameter for particle trapping is the external quantum efficiency (η), defined as

$$\eta = \frac{Q_{\mathrm{rad}}}{Q_{\mathrm{rad}} + Q_{\mathrm{eva}}}, \tag{17}$$

where Q_{rad} and Q_{eva} are the radiated and evanescent power, respectively, dissipated by the particle and calculated as follows,

$$Q_{\mathrm{rad}} = 1 + \frac{\omega}{2\pi}\mathrm{Re}\left\{\iint_R\left(\mathbf{p}^*\cdot\mathbf{E_r^{FT}}\right)dk_xdk_y\right\}, \tag{18}$$

$$Q_{\mathrm{eva}} = \frac{\omega}{4\pi}\mathrm{Re}\left\{\iint_E\left(\mathbf{p}^*\cdot\mathbf{E_r^{FT}}\right)dk_ydk_x\right\}. \tag{19}$$

where R and E are defined as the region inside and outside the circle $|\mathbf{k}_\parallel| \leqslant k_1$, respectively. The large momentum transfer provided by radiative emission can remove a particle from the optical trap. Consequently, it is important to design structures capable of evanescently coupling most of the power emitted by the particle, thereby reducing η. Once the procedure for calculating U and $\langle\mathbf{F}\rangle$ of a nanopatterned structures is complete, the next step is to design the structure capable of trapping a particle modeled by a point dipole.

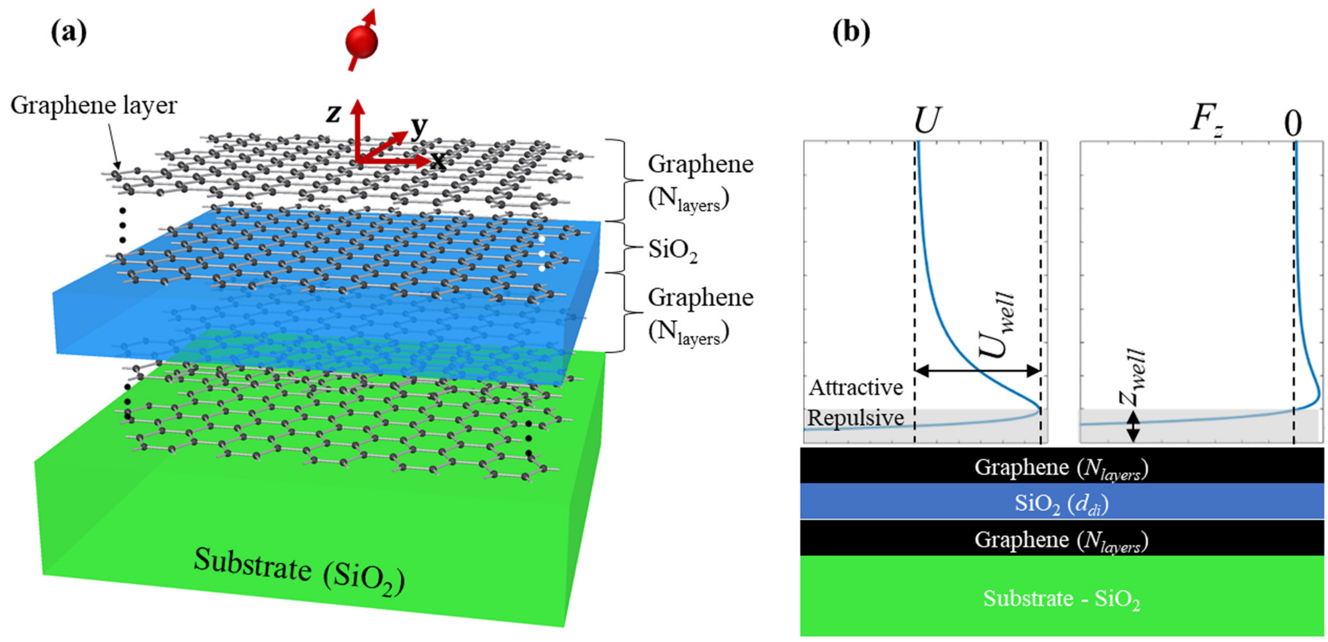

FIG. 2. (a) shows the proposed structure consisting of a thin SiO_2 layer (with thickness d_{di}) sandwiched between N_{layers} layers of graphene. The potential (U) and force (F_z) acting on the particle as a function of the distance z from the proposed structure is presented in (b). U_{well} and z_{well} represent the potential depth and minimum point above the surface, respectively.

III. STRUCTURE DESIGN

The proposed structure consists of a thin SiO_2 layer (with thickness d_{di}) inserted between N_{layers} layers of graphene, as shown in Fig. 2(a). We choose graphene over conventional metals (such as gold and silver) because the thin graphene layers increase k_c [41] and, consequently, enable the force repulsive contribution in the region where $|k_x| < k_c$ to overcome the attractive one, thus allowing the formation of a potential well in some interval of z. The choice for SiO_2 is described in Appendix A. The repulsive force is achieved by applying a potential higher than 1 eV between the graphene layers. With the proposed configuration, the force along the z axis (F_z) is mainly due to the coupling of the evanescent fields with the evanescent bulk modes of the structure. Consequently, F_z is repulsive and decays exponentially as the dipole moves further away from the surface. Note that evanescent waves can be associated with both the dipole and the structure, which might be confusing or misleading. Therefore, to clarify this issue, all the structure modes (evanescent or radiative) are hereafter referred to as "bulk modes," while the term "evanescent fields" refers to the dipole radiation. The exponential decay of the high-k modes responsible for the repulsive force is overcome by the attractive contribution (less attenuated) at $z = z_{\text{well}}$, where the sign of F_z changes and the force acting on the dipole becomes attractive. This creates a stable equilibrium position (EP) which represents the minimum of a potential U_{well} as shown in Fig. 2(b).

To demonstrate how to trap particles with the proposed configuration, we consider a particle with electric polarizability $\alpha = 1.39 \times 10^{-35}\,\mathrm{C\,m^2\,V^{-1}}$ and mass $m = 9.98 \times 10^{-21}$ kg (equivalent to a gold sphere with a 5-nm radius [58]) normally excited from the substrate by a 0.25-W laser with a 12.4-$\mu\mathrm{m}^2$ spot area (equivalent to a 4-μm-diameter monomode fiber) and $\lambda = 780$ nm.The polarizability α and $\mathbf{E_e}$ induce a dipole moment on the gold particle of $p = |\mathbf{p}| = \alpha|\mathbf{E_e}| = 5.43 \times 10^{-29}$ C m. Moreover, the plane excitation wave $[\mathbf{E_e} = E_0 \exp(i\mathbf{k}_1\mathbf{r})\hat{\mathbf{E}}_\mathbf{e}]$ does not contribute to the force $(\mathbf{F_e}(\mathbf{r_d}))$ since the polarizability is assumed lossless $(\mathrm{Im}\{\alpha\} = 0)$ [52,59] and $\nabla E_0 = 0$ (plane wave). The dipolar force on the particle is expressed as follows:

$$\langle \mathbf{F_e}(\mathbf{r_d}) \rangle = \frac{1}{2}\mathrm{Re}\left\{ \sum_{b=x,y,z} i\mathbf{k}_1\alpha^*|E_0|^2 + \alpha^* E_0 \nabla E_0 \right\} = \mathbf{0}. \tag{20}$$

Figure 3 shows the calculated z_{well} (a,d), U_{well} (b,e), and η (c,f) considering a stack composed of a 10-nm silicon dioxide (SiO_2, permittivity 2.16) layer sandwiched between $N_{\text{layers}} = 2$ (squares), 3 (circles), 4 (triangles), 5 (stars), 6 (hollow squares), and 7 (hollow circles) graphene layers for perpendicular $[\mathbf{p} = p\mathbf{z}$, (a–c)] and parallel $[\mathbf{p} = p\mathbf{x}$, (d–f)] polarization. Appendix B contains the graphene properties adopted here. Note that we use temperature units for the potential, whose conversion factor is $U(J) = k_{\text{bol}}T(\mathrm{mK}) \times 10^3$, where k_{bol} is the Boltzmann constant. Furthermore, the graphene Fermi potential is changed with a bias voltage applied to the graphene layers [46,48]. As shown in Appendix A, the repulsive force is present only when the perpendicular ($\varepsilon_\perp$) and parallel ($\varepsilon_\parallel$) permittivities of the graphene-SiO_2-graphene stack, determined according to [41], obey the relation $|\sqrt{\varepsilon_\parallel \varepsilon_\perp}| < 1$, and the force becomes increasingly greater as $|\sqrt{\varepsilon_\parallel \varepsilon_\perp}| \to 0$. This condition is satisfied when E_F becomes higher than a potential threshold (E_T) that depends on the number of graphene layers (see Table I). If $E_F > E_T$, the force becomes repulsive and the well generated by the structure behaves essentially as the one shown in Fig. 2(b).

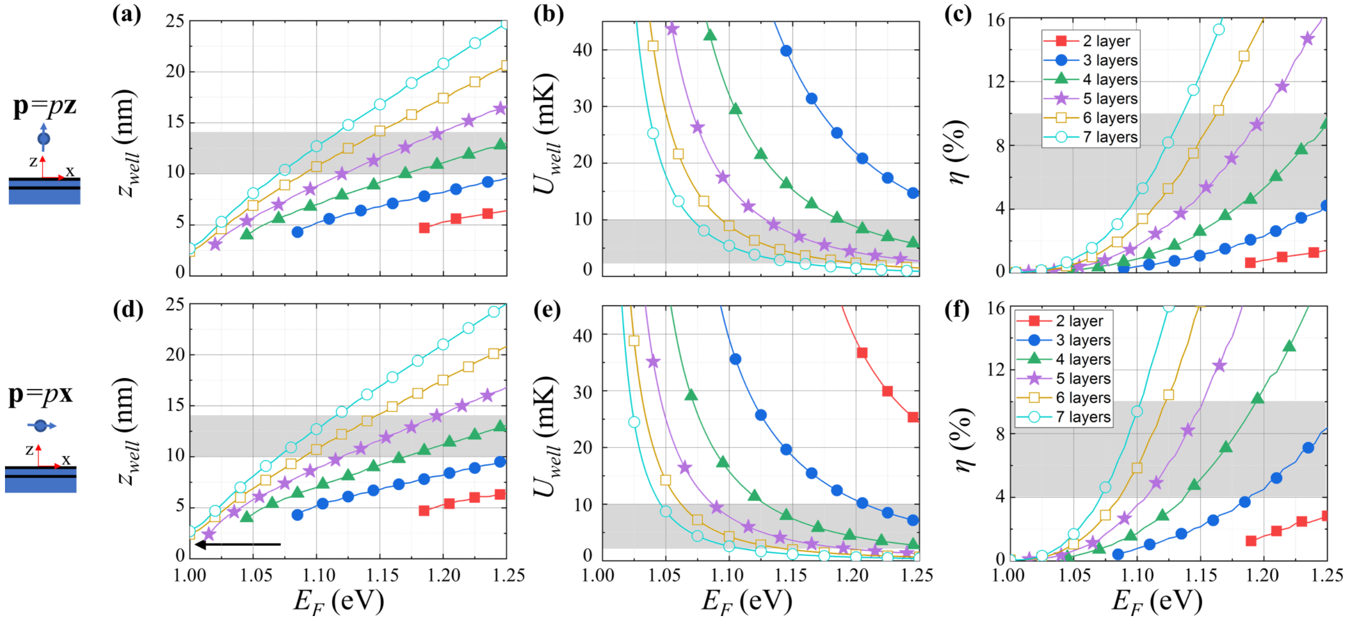

FIG. 3. z_{well} (a,d), U_{well} (b,e), and η (c,f) calculated considering a stack composed of $N_{\text{layers}} = 2$ (squares), 3 (circles), 4 (triangles), 5 (stars), 6 (hollow squares), and 7 (hollow circles) graphene layers for perpendicular [$\mathbf{p} = p\mathbf{z}$, (a–c)] and parallel [$\mathbf{p} = p\mathbf{x}$, (d–f)]. The dipole orientation is shown in the first column.

However, if $E_F > E_T$, the force is attractive, and no potential well is generated. Consequently, z_{well} and U_{well} can only be defined for $E_F > E_T$, as shown in Figs. 3(a) and 3(b). Fewer layers require thinner graphene layers and, consequently, a higher E_F threshold since the graphene would need more free carriers to exhibit a more metallic behavior. Furthermore, when $|\sqrt{\varepsilon_\parallel \varepsilon_\perp}|$ is close to 1 (at the threshold potential), the repulsive force is weak, resulting in an equilibrium position close to the structure surface ($z_{\text{well}} <$ 5nm for $N_{\text{layers}} =$ 2, 3, 4, and 5). As the potential increases, the quantity $|\sqrt{\varepsilon_\parallel \varepsilon_\perp}| \to 0$, causing the repulsive force to increase and z_{well} to move further away from the surface, as shown in Figs. 3(a) and 3(d).

Another important aspect regarding the trapping position is that z_{well} is independent of the dipole polarization, as shown in Figs. 3(a) and 3(d). The reason is that the graphene-SiO$_2$-graphene layers couple mostly p modes. Consequently, the potential energy is defined essentially by p-polarized waves, making the potential minimum position fixed regardless of the dipole orientation. Nevertheless, the well depth is smaller for parallel than for perpendicular polarization because its energy is lost partly as s-polarized waves that do not interact with the structure and therefore do not contribute to the potential depth. The number of layers also plays an important role in the potential well depth, as shown in Figs. 3(b) and 3(e). That is, the greater the number of layers (N_{layers}), the shallower the potential (U) becomes for the same E_F. Furthermore, as N_{layers} increases, the potential well is established further away from the surface (same E_F) and, consequently, the dipole evanescent fields impinging on the structure become weaker. Thus, the coupling to high-k p modes is diminished, resulting in a shallower well. This feature also explains why z_{well} increases while U_{well} decreases for higher E_F, as shown in Figs. 3(b) and 3(e). Moreover, a higher z_{well} implies a higher η because it becomes more difficult for the evanescent waves to couple with the structure modes, as shown in Figs. 3(c) and 3(f). As previously explained, the large momentum transfer provided by the radiative emission might remove the particle from the optical trap. Thus, it might be necessary to lower the quantum efficiency η by either increasing N_{layers} or reducing E_F to prevent the particle from escaping the EP. Unfortunately, the s-polarized waves radiated by the parallel dipole [Fig. 3(f)] do not couple to the bulk modes, and only contribute to the radiative power (Q_{rad}). Note from Figs. 3(c) and 3(f) that η of a parallel dipole is twice as high as that of a perpendicular dipole. This occurs because perpendicular dipoles emit only p-polarized waves, while parallel dipoles emit both s- and p-polarized waves. Finally, either increasing N_{layers} or reducing E_F results in low values of η which helps prevent the particle from escaping the EP.

TABLE I. Potential threshold (E_T) as a function of N_{layers} necessary to generate the potential well.

N_{layers}	2	3	4	5	6	7
E_F (eV)	1.40	1.18	1.08	1.04	1.00	< 1

The stronger coupling between the evanescent waves and the bulk modes results in a deeper U_{well} whenever EP shifts closer to the surface. Although a high U_{well} is desirable, the high power dissipated by the high-k bulk modes enhances the spatial dispersion that modifies the electric field pattern and, consequently, the potential barrier [41]. Hence, the location of EP should be far enough from the surface to avoid spatial dispersion, but close enough to guarantee a potential sufficiently deep to trap particles. These findings show that a range of values for U_{well}, z_{well}, and η must be found to achieve a useful operating region. The following requirements satisfy these conditions:

(1) $z_{\text{well}} >$ 10 nm to avoid spatial dispersion;

(2) $U_{\rm well} > 1$ mK, which is deep enough for small particle trapping applications. Note that larger particles [5,6] demand deeper potential, which is achieved with stronger excitation;

(3) $\eta < 10\%$, to reduce photon emission (assuming particles far from resonances, which reduces the probability of photon emission. Nonetheless, the proposed structure reduces this probability even further).

The gray areas of Figs. 3(a)–3(f) highlight the values of $U_{\rm well}$, $z_{\rm well}$, and η that satisfy these criteria. Note that the range of possible values for $N_{\rm layers}$ and E_F allows structure designs according to fabrication restrictions. Moreover, although thinner graphene layers facilitate the fabrication process, it also requires a higher Fermi potential E_F to satisfy the above criteria. In this sense, to achieve a good compromise between fabrication and performance efficiency, we chose $N_{\rm layers} = 5$ and $E_F = 1.125\,(\mathrm{ev})$. This set of parameters guarantees that the equilibrium position EP is both far enough from the surface to reduce spatial dispersions ($z_{\rm well} = 10\,(\mathrm{nm})$) and deep enough to trap either parallel ($U_{\rm well} = 5.3\,\mathrm{mK}$) or perpendicularly ($U_{\rm well} = 10.5\,\mathrm{mK}$) polarized particles. Moreover, the external quantum efficiency is smaller than 10% regardless of the polarization; i.e., $\eta = 3\%$ and 6% for perpendicularly and parallel polarized particles, respectively.

To gain deeper insight into the nature of the repulsive force, we show in Figs. 4(a)–4(c) the contribution of the spatial distribution of U_z to the force ($U_z = U_r + U_g$) considering $\mathbf{p} = p\mathbf{z}(U_z)$ at distances $q = 8$, 10, and 12 nm from the surface, respectively. To allow clear visualization, Fig. 4(d) shows a cut along the z axis of the U_z map at $x = 0$ (particle-dipole position) for $q = 8$ (circles), 10 (squares), and 12 nm (triangles). Note that, when $q = 8$ nm ($q < z_{\rm well}$), U_z decreases at the particle position, and since the radiation pushes the particle toward the potential minimum, the force is repulsive [red arrow in Fig. 4(d)]. In contrast, when $q = 12$ nm ($q < z_{\rm well}$), U_z at the particle position increases with z, and the force becomes attractive [green arrow in Fig. 4(d)]. Finally, at the EP ($q = 10$ nm), the particle is already at the U_z minimum position, and no net force acts on the particle. Another aspect observed in Figs. 4(a)–4(c) is that the bulk modes excited by the dipole radiation become weaker as the particle moves away from the surface due to the exponential decay of the evanescent fields. Consequently, the absolute value of the force also decreases as indicated by Eq. (1). To understand this phenomenon, the force vector ($\mathbf{F}^{\mathbf{FT}}$) can be written as a function of the spatial frequency ($\mathbf{k}$) as follows,

$$\mathbf{F}^{\mathbf{FT}}(\mathbf{k}_\parallel, \mathbf{r_d}) = \frac{1}{2}\mathrm{Re}\{p_z^* \nabla' E_z^{\mathrm{FT}}(\mathbf{k}_\parallel, \mathbf{r_d})\} + 2\pi \mathbf{F_g}\delta(\mathbf{k}_\parallel), \qquad (21)$$

where ∇' is the del operator in $\mathbf{r_d}$. Figure 4(e) shows the $\mathbf{F}^{\mathbf{FT}}$ z component (F_z^{FT}) normalized to the gravitational force $|\mathbf{F_g}|$, where $k_\rho = \sqrt{k_x^2 + k_y^2}$ is the radial wave vector in cylindrical coordinates (this conversion is possible due to the structure axial symmetry). The total force ($\mathbf{F}$) can be obtained by integrating $\mathbf{F}^{\mathbf{FT}}$ over the full spatial frequency map at the dipole position $\mathbf{r_d}$, as follows:

$$\mathbf{F}(\mathbf{r_d}) = \frac{1}{2\pi}\int_{-\infty}^{\infty}\int_{-\infty}^{\infty}\mathbf{F}^{\mathbf{FT}}(\mathbf{k}_\parallel, \mathbf{r_d})dk_x dk_y. \qquad (22)$$

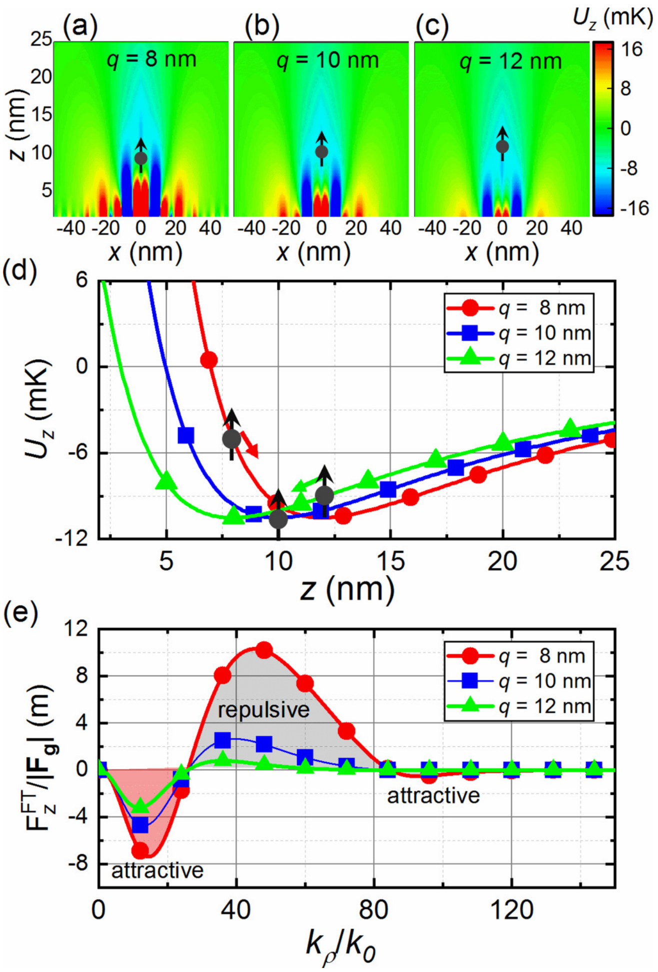

FIG. 4. Spatial distribution U_z for $\mathbf{p} = p\mathbf{z}$ and $q = 8$ (a), 10 (b), and 12 nm (c). (d) represents a cut along the z axis of the U_z map at $x = 0$ (particles position) for $q = 8$ (circles), 10 (squares), and 12 nm (triangles). (e) shows the normalized spatial frequency of the force ($F_z^{\mathrm{FT}}/|\mathbf{F_g}|$) as function of k_ρ for $q = 8$ (circles), 10 (squares), and 12 nm (triangles). In (c), the red and green arrows represent the direction of the force acting on the particle at $q = 8$ and 12 nm, respectively. In (d), the red and black shaded areas represent the regions where the contribution to the force is attractive and repulsive, respectively. The dipole orientation and position are represented by an arrow-crossed solid black circle in (a–d).

According to Fig. 4(e), bulk modes with $k_\rho < 25k_0$ generate attractive forces (red area), while those with $25k_0 < k_\rho < 82k_0$ produce repulsive forces (gray area). The spatial dispersion induced by the layers' thickness creates a cutoff spatial frequency (k_c) at $k_c = 82k_0$, where for $|\sqrt{\varepsilon_\perp \varepsilon_\parallel}| > 1$ with $k_\rho > k_c$ the force becomes attractive. For the proposed structure, the high k_c values allowed by the thin graphene layers make the attractive contribution of $F_z^{\mathrm{FT}}(k_\rho)$ insignificant for $k_\rho > k_c$ [see Eq. (22)]. When the particle is close to the structure ($q < z_{\rm well}$), the repulsive region of $F_z^{\mathrm{FT}}(k_\rho)$ ($25k_0 < k_\rho < 82k_0$) has a higher contribution to the force than its attractive contribution ($25k_0 > k_\rho$), as shown in Fig. 4(e) for $q = 8$ nm (circles). Since F_z is the integral of $F_z^{\mathrm{FT}}(k_\rho)$, F_z becomes repulsive when $q < z_{\rm well}$. As the particle moves further away from the surface, the repulsive contribution

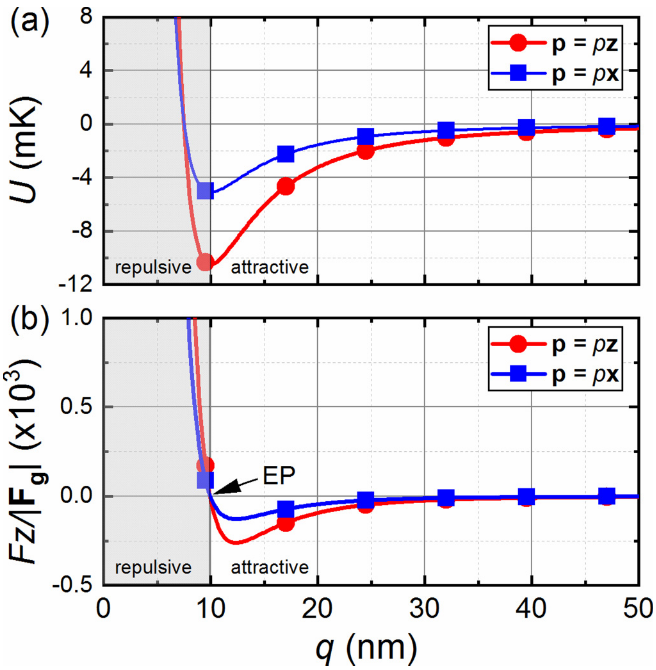

FIG. 5. The potential U (a) and normalized force ($F_z/|\boldsymbol{F}_g|$) as a function of the distance q from the structure for perpendicular (circles) and parallel (squares) polarization. The gray area highlights the region where the force acting on the particles is repulsive.

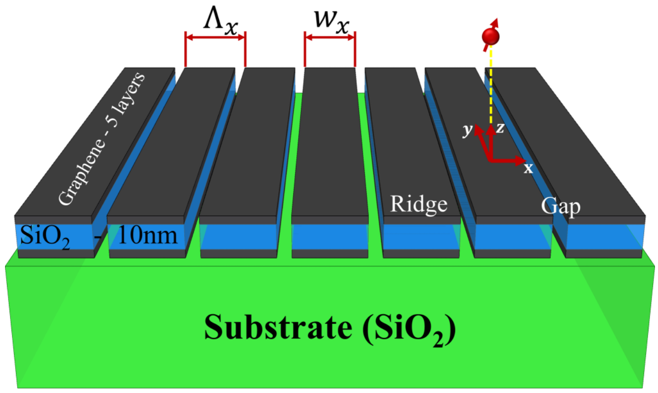

FIG. 6. Optimized graphene-SiO$_2$ stack patterned along the x axis with period (Λ_x) and ridge width (w_x) of 150 and 125 nm, respectively. The optimized structure has a 10-nm-thick SiO$_2$ layer inserted between five graphene layers.

($25k_0 < k_\rho < 82k_0$) is highly attenuated compared to the attractive one ($25k_0 > k_\rho$) due to higher k_ρ, and for $q = 10$ nm (squares), both contributions become equal, resulting in a null force. Note that $F_z^{\rm FT}(k_\rho)$ decays more pronouncedly for $q = 10$ nm than for $q = 8$ nm, as indicated in Figs. 4(a) and 4(b), where U_z is weaker for $q = 10$ nm than for $q = 8$ nm. Furthermore, the higher attenuation of the $F_z^{\rm FT}(k_\rho)$ repulsive contribution results both in an attractive force and a weaker U_z for $q > z_{\rm well}$, as shown in Figs. 4(e) and 4(c). In summary, Fig. 4(e) reveals the role played by the repulsive region higher attenuation (due to higher k_ρ for increasing q) in changing the sign of F_z to produce an EP capable of trapping particles in a potential well. In this sense, Figs. 5(a) and 5(b) show the potential U (circles) and the force along the z direction (F_z), respectively, for a particle located q nm above the structure surface for perpendicular (circles) and parallel (squares) polarizations. Note that U is higher closer to the surface and decreases exponentially for increasing q, as shown in the gray area of Fig. 5(a). This is due to the dipole radiation that couples evanescently to the structure for $q < z_{\rm well}$. Moreover, F_z is positive in this region, causing the force acting on the particle to be repulsive, as shown in the gray area of Fig. 5(b). At $q = z_{\rm well}$, the particle reaches the EP where U is minimum ($U_{\rm well}$) and the force along the z axis is zero ($F_z = 0$). Away from the structure ($q < z_{\rm well}$), U increases smoothly and the force becomes attractive ($F_z < 0$). This behavior is the same for perpendicular and parallel polarizations, except for the amplitudes of U and F_z which are half for parallel polarization (because s-polarized waves do not couple to the structure). Finally, Fig. 5 shows that the designed graphene-based structure can lock the particle position at $z = 10$ nm, regardless of the particle polarization. After delineating the important role played by the high-k bulk modes for the levitation, the next step is to confine the particle along one additional axis.

IV. NANOPATTERNED STRUCTURE ANALYSIS

We accomplish this feature by adding periodic patterns along the x axis of the optimized graphene-SiO$_2$ stack with period $\Lambda_x = 150$ nm and ridge width $w_x = 125$ nm, as depicted in Fig. 6. The optimized structure has a 10-nm-thick SiO$_2$ layer sandwiched between five graphene layers. Figure 7 shows the electric potential (U) generated by the dipole radiation assuming $\mathbf{p} = p\mathbf{z}$ (a), $p\mathbf{x}$ (b), and $p\mathbf{y}$ (c). Similarly to the flat structure in Fig. 2, U increases rapidly close to the surface due to the stronger coupling of evanescent waves with the bulk modes, and decreases exponentialy as the dipole moves further away from the surface. The small magnitude of U above the grooves is explained by the lack of high-k bulk modes to couple with the evanescent waves radiated by the dipole, as shown in Figs. 7(a)–7(c). Furthermore, the $U_{\rm well}$ produced by the patterned structure above the ridges is close to the values obtained with the flat structure ($U_{\rm well} = 9.8$ (mK) and 4.9 mK for $\mathbf{p} = p\mathbf{z}$ and $p\mathbf{x}$ or $p\mathbf{y}$, respectively), and occurs at the same distance from the surface ($z_{\rm well} = 10$ (nm) for $\mathbf{p} = p\mathbf{z}$ $p\mathbf{x}$, or $p\mathbf{y}$). This behavior indicates that the energy reflected by the groove contributes little to U at the ridge center because the coupled high-k bulk modes only project for a few nanometers before being highly attenuated [approximately 35 nm—Figs. 5(a)–5(c)]. As the particle moves from the ridge center toward the groove, the energy reflected by the ridge edges continuously increases, resulting in a potential barrier that constrains the dipole movement along the x axis, as shown in Figs. 7(a)–7(c). Assuming a –3-mK contour [black lines in Figs. 7(a)–7(c)], one obtains a 125-, 100-, and 110-nm-wide well along the x direction, and a 10-, 5-, and 5-nm-wide well along the z direction for $\mathbf{p} = p\mathbf{z}$ $p\mathbf{x}$, or $p\mathbf{y}$, respectively. Note that the barrier width is determined mostly by w_x, whereas the dipole polarization has little to no influence. In summary, the proposed patterned structure is capable of limiting the particle movement along both the z and x axes. A judicious choice of the nanopattern parameters Λ_x and w_x is required to engineer the wells.

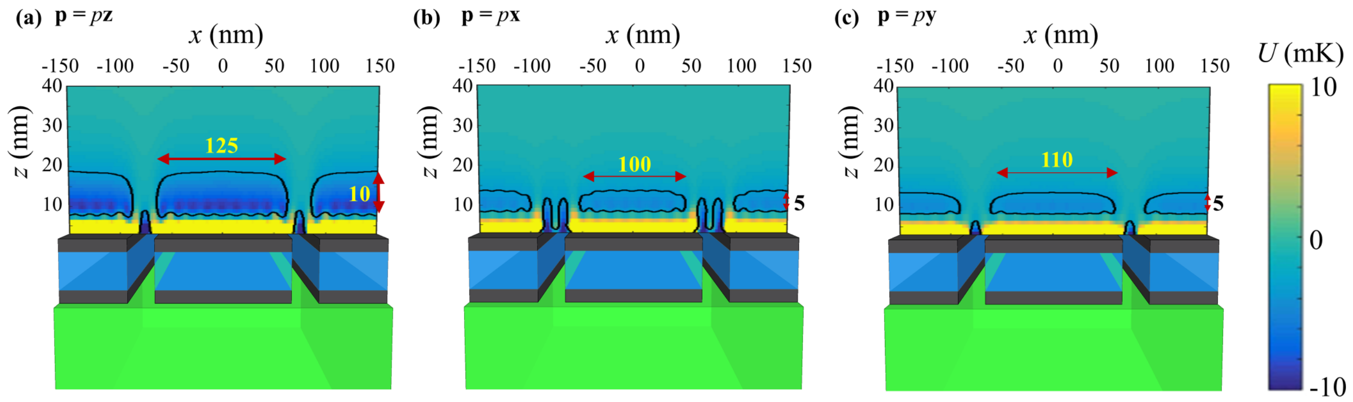

FIG. 7. Electric potential U generated by the particle radiation assuming $\mathbf{p} = p\mathbf{z}$ (a), $p\mathbf{x}$ (b), and $p\mathbf{y}$ (c). The black contours on the potentials delimit the region where $U < –3$ mK in the three panels.

To gain a deeper insight into the the nature of the repulsive force, Figs. 8(a)–8(d) show the spatial distribution of U_z for $\mathbf{p} = p\mathbf{z}$ assuming the dipole at the ridge center ($x_d = 0$) and at $q = 8$ nm (a), 10 nm (b), and 12 nm (c) from the surface. Also assume a dipole close to the –3-mK contour limit at $x_d = -60$ nm for $q = 10$ nm (d). The force direction is shown as a red arrow. Due to symmetry, the force along the x direction is null for these three positions. Furthermore, as the force direction indicates, the particle tends to move toward the minimum of U_z, representing a repulsive force for $q = 8$ nm ($F_z = 1.1 \times 10^3|\mathbf{F_g}|$), a nearly null force for $q = 10$ nm ($F_z = 630|\mathbf{F_g}|$), and an attractive force for $q = 12$ nm ($F_z = –0.2 \times 10^3|\mathbf{F_g}|$). This force behavior results in the potential observed at Fig. 7(a). As in the flat structure, the amplitude of U_z decreases as the particle moves away from the surface due to exponential decay of the evanescent field. This property can be further understood by analyzing $F_z^{\rm FT}$ shown in Figs. 8(e)–8(g) for $x_d = 0$ (nm) and $q = 8$, 10, and 12 nm, respectively. These figures show that the high-k bulk modes are repulsive for $|\mathbf{k}_\parallel/k_0| \geqslant 25$ and attractive for $|\mathbf{k}_\parallel/k_0| < 25$. Closer to the surface ($q < z_{\rm well}$), the integral of the repulsive contribution is higher than the attractive counterpart resulting in repulsive F_z ($q = 8$ nm). Further away from the surface ($q < z_{\rm well}$), the attractive contribution overcomes the repulsive one due to the higher attenuation of the modes with $|\mathbf{k}_\parallel/k_0| \geqslant 25$. F_z is close to zero where the contribution of both regions is equal, and no force acts on the particle. Figures 8(i)–8(k) show the spatial frequency dependence of the force along the x direction ($F_x^{\rm FT}$) for $x_d = 0$ for $q = 8$, 10, and 12 nm, respectively. The force acts pushing the particle to the right (positive values) when $k_x/k_0 > 0$ and to the left (negative values) when $k_x/k_0 < 0$, as shown in Figs. 8(i)–8(k). These forces become equal and cancel due to the structure symmetry, resulting in $F_x = 0$ when the dipole is located at the ridge center. Note that $F_x^{\rm FT}$ is weaker when the particle is further away from the structure. However, since the positive and negative contributions cancel, their influence on F_x is not as strong as it is on F_z. An interesting phenomenon occurs when the particle is located close to the −3-mK contour, i.e., at $\boldsymbol{x_d} = –60$ nm and $q = 10$ nm. At this position, the influence of the groove (62.5 nm $< x <$ –75 nm) on U_z shifts the potential minimum to the right side of the particle, thus pushing the particles toward the $+\mathbf{x}$ direction, as depicted in Fig. 8(d). Furthermore, the groove also disturbs $F_z^{\rm FT}$ and $F_x^{\rm FT}$, as shown in Figs. 8(h) and 8(l), respectively. The groove makes it physically more difficult for the high-k bulk modes ($k_x < 0$) to project into the space above the surface (especially for $|\mathbf{k}_\parallel/k_0| \geqslant 25$), which, particularly for $F_z^{\rm FT}$, reduces the repulsive contribution of the force resulting in a net F_z attractive force [see Figs. 8(d) and 8(h)]. For the same reason, the contribution of $F_x^{\rm FT}$ to the right gets stronger ($k_x > 0$), resulting in a positive force pushing the particles toward the ridge center [see Figs. 8(d) and 8(h)]. In summary, any particle's movement away from the EP ($x_d = 0$ and $q = 10$ nm), either in the x or z direction, disturbs $F_x^{\rm FT}$ and $F_z^{\rm FT}$ in such way as to generate a force that pushes the particle to the EP. Therefore, the structure generates a potential well capable of trapping small particles in a stable transversal and longitudinal equilibrium.

We have chosen graphene due to both its small thickness (helps increase k_c) and conductivity (varies with external bias voltage). This property allows us to dynamically control the trapping position by individually adjusting the applied voltage on each graphene ridge. It should be emphasized that to realize the electric contacts, the patterning must be created along one axis only (x axis here); otherwise the contacts would be segmented, making it difficult to electrically connect the inner ridges. In the event this limitation is overcome (with a proper choice of materials and fabrication technology), our semianalytical model could still be used to design and optimize a structure that ultimately would be capable of trapping in three dimensions.

V. CONCLUSIONS

In this paper, we have proposed an approach for particle trapping/levitation (based on the point dipole scattered radiation) and a semianalytical method to calculate the potentials and forces generated by a particle radiation located above a nanopatterned structure. With this formalism, we have optimized a realistic nanopatterned graphene-based structure capable of trapping small particles located above the structure. We have also demonstrated how to control the trapping position by adjusting E_F and the number of graphene layers. Based on this control, we have optimized the structure to achieve a deep well ($U_{\rm well}$ $U_{\rm well} = 10.5$ mK for the dipole alignment perpendicular to the surface or 5.3 mK for parallel

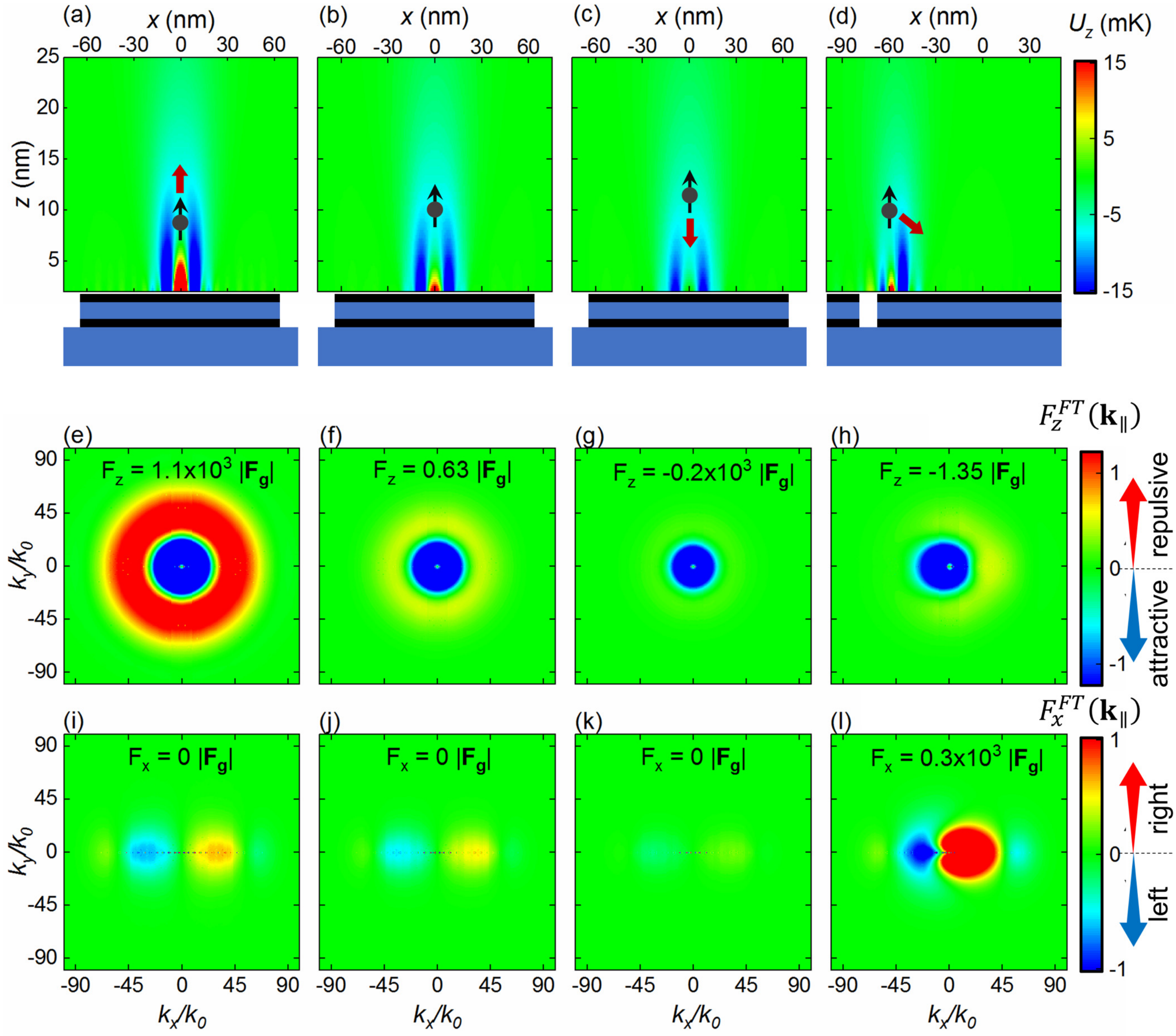

FIG. 8. Spatial distribution of $\boldsymbol{U}_z$ for $\mathbf{p} = p\mathbf{z}$ assuming the dipole at the ridge center ($x_d = 0$) and at $q = 8$ nm (a), 10 nm (b), and 12 nm (c) from the surface. The red arrows in (a,c,d) represent the force direction. The spectral distribution of (F_z^{FT}, F_x^{FT}) is shown for $x_d = 0$ (nm) and $q = 8$ nm (a,i), 10 nm (b,j), and 12 nm (c,k) and for $x_d = -60$ nm and $q = 10$ nm (d,l). The structure cross section is shown below (a–d) and, for comparison sake, both (F_z^{FT}, F_x^{FT}) are normalized to $|\mathbf{F}_\mathrm{g}|/k_0 \times 10^{-7}$ to match those for $\mathbf{F}^{\mathbf{FT}}(k_\rho)$ in Fig. 4(d). In (d), the structure is shifted along the x axis to emphasize the field close to the groove and the force imbalance in (h,l).

alignment) whose minimum is far enough from the surface ($z_{\mathrm{well}} = 10$ nm) to reduce the attractive contribution of the evanescent waves. Moreover, a deeper potential for larger particle trapping can be achieved with stronger light excitation. Using the proposed semianalytical method, we have described the influence of the high-k modes on the repulsive ($k_\rho > 25k_0$) and attractive forces ($k_\rho < 25k_0$) acting on the particle. Based on this influence, we have also explained why the force becomes repulsive for $q < z_{\mathrm{well}}$ and attractive otherwise. We have then added 150-nm periodic grooves on the optimized structure (with $w_r = 125$ (nm)) to bind the particle movement along the x axis. Our results reveal that close to the ridge center, the groove has little to no influence on U due to attenuation of the high-k modes, and the force resembles that of the nonpatterned structure. As the particle moves toward the groove, the scattered waves unbalance the lateral forces, resulting in a force that acts as a restoring force on the dipole, limiting its movement along the x axis. It is important to emphasize that the semianalytical method allows the calculation of the spatial spectrum of both the potential well and the force acting on a particle above any nanopatterned structure, thus providing valuable insights into the contribution of the high-k bulk modes to particle trapping. It also allows confinement optimization along one, two, or three axes for a generalized patterned structure. Combining the semianalytical method with optimization algorithms, such as machine learning and genetic algorithms, among others, would be straightforward. Our outcomes have direct applications to optical trapping, optical tracking, quantum cooling, and electromagnetic levitation.

ACKNOWLEDGMENTS

This work was funded by Conselho Nacional de Desenvolvimento Científico e Tecnológico (PQ 303562/2017-0), FAPESP (Grants No. 2013/07276-1 and No. 2015/21455-1). The authors would like to acknowledge the computational support of the Núcleo de Apoio á Óptica e Fotŏnica (NAPOF/USP).

APPENDIX A

Here, we discuss the necessary conditions for a biaxial homogeneous anisotropic medium with permittivity and permeability tensors described as $\mathrm{diag}[\varepsilon_\parallel;\varepsilon_\parallel;\varepsilon_\perp]$ and $\mathrm{diag}[\mu_\parallel;\mu_\parallel;\mu_\perp]$, respectively, to generate repulsive forces. Assuming a particle in vacuum above the described media, the contribution of the particle s- and p-polarized wave emissions is repulsive when $\mathrm{Re}\{r_{p,p}^{0,0}\,(|\mathbf{k}_\parallel|)\} < 0$ and $\mathrm{Re}\{r_{s,s}^{0,0}|\mathbf{k}_\parallel|\} < 0$ in the quasistatic regime ($\mathbf{k}_\parallel \gg k_0$) [13]. We substitute the definition of $r_{p,p}^{0,0}$ and $r_{s,s}^{0,0}$ [41] into the inequalities,

$$\mathrm{Re}\left\{\frac{\frac{\varepsilon_\parallel\sqrt{k_0^2-|\mathbf{k}_\parallel|}^2}{\sqrt{k_0^2\mu_\parallel\varepsilon_\parallel-\frac{\varepsilon_\parallel}{\varepsilon_\perp}|\mathbf{k}_\parallel|^2}}-1}{\frac{\varepsilon_\parallel\sqrt{k_0^2-|\mathbf{k}_\parallel|}^2}{\sqrt{k_0^2\mu_\parallel\varepsilon_\parallel-\frac{\varepsilon_\parallel}{\varepsilon_\perp}|\mathbf{k}_\parallel|^2}}+1}\right\} < 0 \xrightarrow{|\mathbf{k}_\parallel|\gg k_0} \mathrm{Re}\left\{\frac{\sqrt{\varepsilon_\parallel\varepsilon_\perp}-1}{\sqrt{\varepsilon_\parallel\varepsilon_\perp}+1}\right\}$$

$$< 0 => \left|\sqrt{\varepsilon_\parallel\varepsilon_\perp}\right| < 1, \qquad \text{(A1)}$$

$$\mathrm{Re}\left\{\frac{\frac{\mu_\parallel\sqrt{k_0^2-|\mathbf{k}_\parallel|}^2}{\sqrt{k_0^2\mu_\parallel\varepsilon_\parallel-\frac{\mu_\parallel}{\mu_\perp}|\mathbf{k}_\parallel|^2}}-1}{\frac{\mu_\parallel\sqrt{k_0^2-k_x^2}}{\sqrt{k_0^2\mu_\parallel\varepsilon_\parallel-\frac{\mu_\parallel}{\mu_\perp}|\mathbf{k}_\parallel|^2}}+1}\right\} < 0 \xrightarrow{|\mathbf{k}_\parallel|\gg k_0} \mathrm{Re}\left\{\frac{\sqrt{\mu_\parallel\mu_\perp}-1}{\sqrt{\mu_\parallel\mu_\perp}+1}\right\}$$

$$< 0 => \left|\sqrt{\mu_\parallel\mu_\perp}\right| < 1. \qquad \text{(A2)}$$

Based on (A1) and (A2), the contributions of p- and s-polarized waves are repulsive if the medium parameters obey the relations $|\sqrt{\varepsilon_\parallel\varepsilon_\perp}| < 1$ and $|\sqrt{\mu_\parallel\mu_\perp}| < 1$, respectively. Nonetheless, when the particle is oriented perpendicularly to the medium surface, the emission consists only of p waves [see Eqs. (5)–(9). Therefore $|\sqrt{\varepsilon_\parallel\varepsilon_\perp}| < 1$ is condition enough to exhibit a repulsive force. Moreover, the p- and s-polarization contributions to the force modulus are proportional to $|r_{p,p}^{0,0}|$ and $|r_{s,s}^{0,0}|$, respectively. Consequently, a medium with $|\sqrt{\varepsilon_\parallel\varepsilon_\perp}| < 1$ that also allows surface plasmon polariton ($|r_{p,p}^{0,0}| \gg |r_{s,s}^{0,0}|$) would generate repulsive forces, even if violating the condition $|\sqrt{\mu_\parallel\mu_\perp}| < 1$. One approach to creating a medium with those properties is by stacking alternating thin ($<\lambda/10$) layers of metallic and dielectric materials. Since the metallic (d_m) and dielectric (d_d) thicknesses are much smaller than λ, the medium behaves as a biaxial homogeneous anisotropic material [30,31,41]. Furthermore, by controlling the metal and dielectric thicknesses and permittivities (ε_m and ε_d) it is possible to control both $\varepsilon_\parallel$ [$\varepsilon_\parallel = f\varepsilon_\mathrm{m} + (1-f)\varepsilon_\mathrm{d}$] and $\varepsilon_\perp$ [$\varepsilon_\perp = \frac{\varepsilon_\mathrm{d}\varepsilon_\mathrm{m}}{f\varepsilon_\mathrm{d}+(1-f)\varepsilon_\mathrm{m}}$], where f is the metallic fill fraction ($f = d_m/[d_m + d_d]$); d_m and d_d are the thickness of the metal and dielectric layers, respectively.

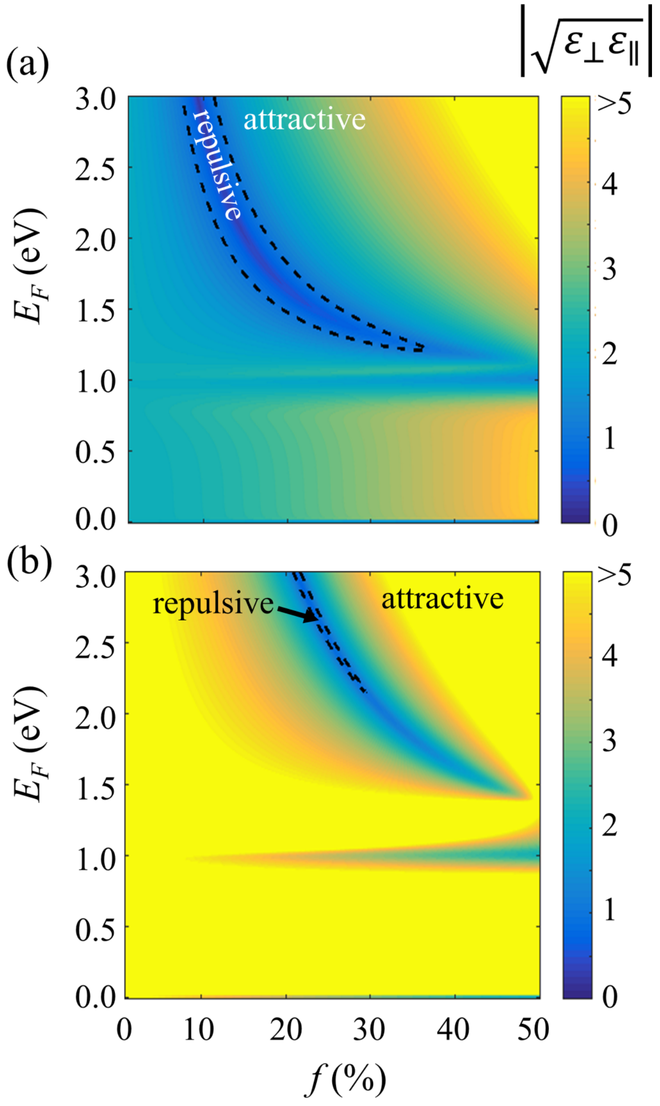

FIG. 9. (a) shows the calculated $|\sqrt{\varepsilon_\parallel\varepsilon_\perp}|$ for a stack of SiO$_2$ ($\varepsilon_d = 2.16$) and graphene for different filling factors (f) and Fermi potential (E_F). (b) shows the calculated $|\sqrt{\varepsilon_\parallel\varepsilon_\perp}|$ for a stack of TiO$_2$ ($\varepsilon_d = 4.39$) and graphene for different f and E_F.

The use of graphene sheets as the metallic material adds a new parameter for controlling the homogeneous permittivity because it is possible to control ε_m by changing the graphene Fermi level (E_F). To find the best dielectric material, we tested $|\sqrt{\varepsilon_\parallel\varepsilon_\perp}|$ both for a stack composed of graphene and titanium dioxide (TiO$_2$ $\varepsilon_d = 4.39$ at $\lambda = 780$ nm), and for graphene and silicon dioxide (SiO$_2$, $\varepsilon_d = 2.16$ at $\lambda = 780$ nm). Knowing that the goal of this calculation is to decide the best dielectric material, the graphene is assumed isotropic for the sake of simplicity. Figures 9(a) and 9(b) show $|\sqrt{\varepsilon_\parallel\varepsilon_\perp}|$ for different values of E_F and f for SiO$_2$ and TiO$_2$, respectively. The black dashed line delimits the region where $|\sqrt{\varepsilon_\parallel\varepsilon_\perp}| < 1$ and the force is repulsive. As Fig. 9(b) shows, the use of TiO$_2$ demands high E_F to achieve repulsive forces ($E_F > 2.1$eV). Also, the repulsive region is narrower in this case, meaning that a more accurate fabrication method is required to achieve a specific f. Note in Fig. 9(a) that when using $\mathrm{SiO_2}$, the repulsive region becomes wider, requiring a lower E_F ($E_F > 1.1\,\mathrm{eV}$). Also, a lower f becomes necessary, which is desirable because it implies a lower number of graphene layers. For this reason, we decided to use $\mathrm{SiO_2}$ in the proposed structure. We have also tested other dielectric materials (Si, $\mathrm{GeO_2}$), but low-refractive-index materials have presented better results.

APPENDIX B

The graphene conductivity (σ_{graph}) of a single sheet is modeled by the local ($|\mathbf{k}_\parallel| = 0$) random-phase-approximation (RPA) [46–48,60,61] as follows,

$$\sigma_{\mathrm{graph}}(\omega) = \frac{e^2}{\pi\hbar^2}\frac{i}{(\omega + i\tau^{-1})} \times \left\{E_F^T - \int_0^\infty dE\, \frac{f_E - f_{-E}}{1 - E^2/[\hbar^2(\omega + j\tau^{-1})^2]}\right\}, \tag{B1}$$

where E_F^T is the Fermi energy (E_F) corrected by the temperature as follows,

$$E_F^T = E_F + 2k_BT\log(1 + e^{-E_F/k_BT}), \tag{B2}$$

$$\tau = \mu E_F/ev_F^2, \tag{B3}$$

$$f_E = \frac{1}{1 + e^{(E-E_F)/k_BT}}, \tag{B4}$$

where e is the electron charge, T is the temperature, μ is the mobility, and v_F is the graphene Fermi velocity. Throughout this paper, we have assumed $T = 300\,\mathrm{K}$, $\mu = 2000\,\mathrm{cm^2/V\,s}$, and $v_F = 10^6\,\mathrm{m/s}$ [48]. Moreover, the Fermi wavelength ($\lambda_F = 2\pi/k_F \sim$ 4–10 m) is much smaller than the operational wavelength ($\lambda = 780\,\mathrm{nm}$). Thus the nonlocal effects in the graphene conductivity are disregarded in this work (more details about this can be found in [46–48]). The total conductivity of an N-layer graphene stack is $\sigma_N = N\sigma_{\mathrm{graph}}$ [62]. To apply the graphene conductivity in the RCWA method, we turn the graphene stack into a homogeneous biaxial medium with parallel ($\varepsilon_x^{\mathrm{graph}}$) and perpendicular ($\varepsilon_y^{\mathrm{graph}}$) components of the permittivity tensor described as [46,63]

$$\varepsilon_{x,y}^{\mathrm{graph}} = 1 + i\frac{\sigma_N}{\varepsilon_0 N d_{\mathrm{layer}}}, \tag{B5}$$

$$\varepsilon_z^{\mathrm{graph}} = 1, \tag{B6}$$

where d_{graph} is the thickness of a single graphene layer assumed here as 0.3 nm [46].

[1] T. K. Langin, G. M. Gorman, and T. C. Killian, Laser cooling of ions in a neutral plasma, Science **363**, 61 (2019).

[2] K. C. Neuman and S. M. Block, Optical trapping, Rev. Sci. Instrum. **75**, 2787 (2004).

[3] H. Bender, P. W. Courteille, C. Marzok, C. Zimmermann, and S. Slama, Direct Measurement of Intermediate-Range Casimir-Polder Potentials, Phys. Rev. Lett. **104**, 083201 (2010).

[4] T. M. Grzegorczyk, B. A. Kemp, and J. A. Kong, Stable Optical Trapping Based on Optical Binding Forces, Phys. Rev. Lett. **96**, 113903 (2006).

[5] D. Windey, C. Gonzalez-Ballestero, P. Maurer, L. Novotny, O. Romero-Isart, and R. Reimann, Cavity-Based 3D Cooling of a Levitated Nanoparticle via Coherent Scattering, Phys. Rev. Lett. **122**, 123601 (2019).

[6] U. Delić, M. Reisenbauer, D. Grass, N. Kiesel, V. Vuletić, and M. Aspelmeyer, Cavity Cooling of a Levitated Nanosphere by Coherent Scattering, Phys. Rev. Lett. **122**, 123602 (2019).

[7] C. Monroe and J. Kim, Scaling the ion trap quantum processor, Science **339**, 1164 (2013).

[8] F. Merola, P. Memmolo, L. Miccio, V. Bianco, M. Paturzo, and P. Ferraro, Diagnostic tools for lab-on-chip applications based on coherent imaging microscopy, Proc. IEEE **103**, 192 (2015).

[9] E. H. Brandt, Levitation in physics, Science **243**, 349 (1989).

[10] M. G. Silveirinha, S. A. H. Gangaraj, G. W. Hanson, and M. Antezza, Fluctuation-induced forces on an atom near a photonic topological material, Phys. Rev. A **97**, 022509 (2018).

[11] R. Zhao, L. Li, S. Yang, W. Bao, Y. Xia, P. Ashby, Y. Wang, and X. Zhang, Stable Casimir equilibria and quantum trapping, Science **364**, 984 (2019).

[12] A. Ivinskaya, N. Kostina, A. Proskurin, M. I. Petrov, A. A. Bogdanov, S. Sukhov, A. V. Krasavin, A. Karabchevsky, A. S. Shalin, and P. Ginzburg, Optomechanical manipulation with hyperbolic metasurfaces, ACS Photonics **5**, 4371 (2018).

[13] F. J. Rodríguez-Fortuño, A. Vakil, and N. Engheta, Electric Levitation Using ϵ-Near-Zero Metamaterials, Phys. Rev. Lett. **112**, 033902 (2014).

[14] D. G. Grier, A revolution in optical manipulation, Nature **424**, 810 (2003).

[15] H. Zheng, X. Yu, W. Lu, J. Ng, and Z. Lin, GCforce: Decomposition of optical force into gradient and scattering parts, Comput. Phys. Commun. **237**, 188 (2019).

[16] A. Ashkin and J. M. Dziedzic, Optical levitation by radiation pressure, Appl. Phys. Lett. **19**, 283 (1971).

[17] A. Ashkin, J. M. Dziedzic, J. E. Bjorkholm, and S. Chu, Observation of a single-beam gradient force optical trap for dielectric particles, Opt. Lett. **11**, 288 (1986).

[18] V. Ginis, P. Tassin, C. M. Soukoulis, and I. Veretennicoff, Enhancing Optical Gradient Forces with Metamaterials, Phys. Rev. Lett. **110**, 057401 (2013).

[19] X. Yang, Y. Liu, R. F. Oulton, X. Yin, and X. Zhang, Optical forces in hybrid plasmonic waveguides, Nano Lett. **11**, 321 (2011).

[20] A. Oskooi, P. A. Favuzzi, Y. Kawakami, and S. Noda, Tailoring repulsive optical forces in nanophotonic waveguides, Opt. Lett. **36**, 4638 (2011).

[21] K. Diniz, R. S. Dutra, L. B. Pires, N. B. Viana, H. M. Nussenzveig, and P. A. Maia Neto, Negative optical torque on a microsphere in optical tweezers, Opt. Express **27**, 5905 (2019).

[22] H. Q. Quy, D. Q. Tuan, T. D. Thanh, and N. M. Thang, Enhance of optical trapping efficiency by nonlinear optical tweezers, Opt. Commun. **427**, 341 (2018).

[23] M. L. Juan, M. Righini, and R. Quidant, Plasmon nano-optical tweezers, Nat. Photonics **5**, 349 (2011).

[24] F. J. Rodríguez-Fortuño, N. Engheta, A. Martínez, and A. V. Zayats, Lateral forces on circularly polarizable particles near a surface, Nat. Commun. **6**, 8799 (2015).

[25] S. A. Hassani Gangaraj, G. W. Hanson, M. Antezza, and M. G. Silveirinha, Spontaneous lateral atomic recoil force close to a photonic topological material, Phys. Rev. B **97**, 201108(R) (2018).

[26] J. J. Kingsley-Smith, M. F. Picardi, L. Wei, A. V Zayats, and F. J. Rodríguez-Fortuño, Optical forces from near-field directionalities in planar structures, Phys. Rev. B **99**, 235410 (2019).

[27] F. Intravaia, C. Henkel, and M. Antezza, Fluctuation-induced forces between atoms and surfaces: The casimir-polder interaction, in *Casimir Physics*, Lecture Notes in Physics Vol. 834, edited by D. Dalvit, P. Milonni, D. Roberts, and F. da Rosa (Springer, Berlin, 2011), pp. 345–391.

[28] M. Boström, M. Dou, O. I. Malyi, P. Parashar, D. F. Parsons, I. Brevik, and C. Persson, Fluid-sensitive nanoscale switching with quantum levitation controlled by α-Sn/β-Sn phase transition, Phys. Rev. B **97**, 125421 (2018).

[29] H. F. Arnoldus and Z. Xu, Force on an electric dipole near an ENZ interface, J. Opt. Soc. Am. B **36**, F18 (2019).

[30] A. F. da Mota, A. Martins, V. Pepino, H. Ottevaere, W. Meulebroeck, F. L. Teixeira, and B.-H. V. Borges, Semianalytical modeling of arbitrarily distributed quantum emitters embedded in nanopatterned hyperbolic metamaterials, J. Opt. Soc. Am. B **36**, 1273 (2019).

[31] A. F. da Mota, A. Martins, H. Ottevaere, W. Meulebroeck, E. R. Martins, J. Weiner, F. L. Teixeira, and B.-H. V. Borges, Semianalytical model for design and analysis of grating-assisted radiation emission of quantum emitters in hyperbolic metamaterials, ACS Photonics **5**, 1951 (2018).

[32] I. Liberal and N. Engheta, Near-zero refractive index photonics, Nat. Photonics **11**, 149 (2017).

[33] N.-H. Shen, P. Zhang, T. Koschny, and C. M. Soukoulis, Metamaterial-based lossy anisotropic epsilon-near-zero medium for energy collimation, Phys. Rev. B **93**, 245118 (2016).

[34] M. Silveirinha and N. Engheta, Design of matched zero-index metamaterials using nonmagnetic inclusions in epsilon-near-zero media, Phys. Rev. B **75**, 075119 (2007).

[35] A. Poddubny, I. Iorsh, P. A. Belov, and Y. Kivshar, Hyperbolic metamaterials, Nat. Photonics **7**, 948 (2013).

[36] C. L. Cortes, W. Newman, S. Molesky, and Z. Jacob, Quantum nanophotonics using hyperbolic metamaterials, J. Opt. **14**, 063001 (2012).

[37] A. V. Chebykin, A. A. Orlov, A. S. Shalin, A. N. Poddubny, and P. A. Belov, Strong Purcell effect in anisotropic ε-near-zero metamaterials, Phys. Rev. B **91**, 205126 (2015).

[38] L. Ferrari, J. Smalley, Y. Fainman, and Z. Liu, Hyperbolic metamaterials for dispersion-assisted directional light emission, Nanoscale **9**, 9034 (2017).

[39] G. T. Papadakis, D. Fleischman, A. Davoyan, P. Yeh, and H. A. Atwater, Optical magnetism in planar metamaterial heterostructures, Nat. Commun. **9**, 296 (2018).

[40] A. V. Chebykin, A. A. Orlov, C. R. Simovski, Y. S. Kivshar, and P. A. Belov, Nonlocal effective parameters of multilayered metal-dielectric metamaterials, Phys. Rev. B **86**, 115420 (2012).

[41] A. F. Mota, A. Martins, J. Weiner, F. L. Teixeira, and Ben-Hur V. Borges, Constitutive parameter retrieval for uniaxial metamaterials with spatial dispersion, Phys. Rev. B **94**, 115410 (2016).

[42] G. T. Papadakis, P. Yeh, and H. A. Atwater, Retrieval of material parameters for uniaxial metamaterials, Phys. Rev. B **91**, 155406 (2015).

[43] M. Mahmoodi, S. H. Tavassoli, O. Takayama, J. Sukham, R. Malureanu, and A. V. Lavrinenko, Existence conditions of high-k modes in finite hyperbolic metamaterials, Laser Photonics Rev. **13**, 1800253 (2019).

[44] V. Popov, A. V. Lavrinenko, and A. Novitsky, Operator approach to effective medium theory to overcome a breakdown of Maxwell Garnett approximation, Phys. Rev. B **94**, 085428 (2016).

[45] F. J. Rodríguez-Fortuño, M. F. Picardi, and A. V. Zayats, Repulsion of polarized particles from two-dimensional materials, Phys. Rev. B **97**, 205401 (2018).

[46] F. J. García de Abajo, Graphene plasmonics: Challenges and opportunities, ACS Photonics **1**, 135 (2014).

[47] Y. D. Kim, Y. Gao, R. Shiue, L. Wang, O. B. Aslan, M. Bae, H. Kim, D. Seo, H. Choi, S. H. Kim, A. Nemilentsau, T. Low, C. Tan, D. K. Efetov, T. Taniguchi, K. Watanabe, K. L. Shepard, T. F. Heinz, D. Englund, and J. Hone, Ultrafast graphene light emitters, Nano Lett. **18**, 934 (2018).

[48] R. Yu, V. Pruneri, and F. J. García de Abajo, Resonant visible light modulation with graphene, ACS Photonics **2**, 550 (2015).

[49] A. Manjavacas, F. J. Rodríguez-Fortuño, F. J. García de Abajo, and A. V. Zayats, Lateral Casimir Force on a Rotating Particle near a Planar Surface, Phys. Rev. Lett. **118**, 133605 (2017).

[50] H. Nyquist, Thermal agitation of electric charge in conductors, Phys. Rev. **32**, 110 (1928).

[51] H. B. Callen and T. A. Welton, Irreversibility and generalized noise, Phys. Rev. **83**, 34 (1951).

[52] R. Grimm, M. Weidemüller, and Y. B. Ovchinnikov, Optical dipole traps for neutral atoms, Adv. At., Mol., Opt. Phys. **42**, 95 (2000).

[53] L. Novotny and B. Hecht, *Principles of Nano-Optics*, 2nd ed. (Cambridge University Press, Cambridge, 2006).

[54] D. M. Whittaker and I. S. Culshaw, Scattering-matrix treatment of patterned multilayer photonic structures, Phys. Rev. B **60**, 2610 (1999).

[55] E. Popov and M. Nevière, Maxwell equations in Fourier space: Fast-converging formulation for diffraction by arbitrary shaped, periodic, anisotropic media, J. Opt. Soc. Am. A **18**, 2886 (2001).

[56] M. Liscidini, D. Gerace, L. C. Andreani, and J. E. Sipe, Scattering-matrix analysis of periodically patterned multilayers with asymmetric unit cells and birefringent media, Phys. Rev. B **77**, 035324 (2008).

[57] C. David, J. Christensen, and N. A. Mortensen, Spatial dispersion in two-dimensional plasmonic crystals: Large blueshifts promoted by diffraction anomalies, Phys. Rev. B **94**, 165410 (2016) .

[58] J. D. Jackson, *Classical Electrodynamics* (Wiley, New York, 1989).

[59] V. Astapenko, *Polarization Bremsstrahlung on Atoms, Plasmas, Nanostructures and Solids* (Springer, Berlin, Heidelberg, 2013).

[60] B. Wunsch, T. Stauber, F. Sols, and F. Guinea, Dynamical polarization of graphene at finite doping, New J. Phys. **8**, 318 (2006).

[61] E. H. Hwang and S. Das Sarma, Dielectric function, screening, and plasmons in two-dimensional graphene, Phys. Rev. B **75**, 205418 (2007).

[62] H. Min and A. H. MacDonald, Origin of Universal Optical Conductivity and Optical Stacking Sequence Identification in Multilayer Graphene, Phys. Rev. Lett. **103**, 067402 (2009).

[63] L. A. Falkovsky, Optical properties of graphene, J. Phys.: Conf. Ser. **129**, 012004 (2008).